---

**Article:**
Magnus, C., Sharp, J. orcid.org/0000-0001-8168-8422 and Rainforth, W.M. orcid.org/0000-0003-3898-0318 (2019) The lubricating properties of spark plasma sintered (SPS) Ti3SiC2 MAX phase compound and composite. Tribology Transactions, 63 (1). pp. 38-51. ISSN 1040-2004

https://doi.org/10.1080/10402004.2019.1657534

---

# The lubricating properties of spark plasma sintered (SPS) $Ti_3SiC_2$ MAX phase compound and composite

Carl Magnus, Joanne Sharp, and William M. Rainforth

Department of Materials Science and Engineering, The University of Sheffield, Mappin Street, Sheffield S1 3JD, UK.

## ABSTRACT

MAX phase composites $Ti_3SiC_2$ – TiCx and $Ti_3SiC_2$ – ($TiC_X$ + TiC) were synthesized and consolidated via the powder metallurgy spark plasma sintering (SPS) technique. The bulk compositions and microstructural evolution of the resulting SPS discs were analysed using X-ray diffraction, Raman spectroscopy and scanning electron microscopy with EDS. The tribological behaviour of the synthesized discs was investigated at room temperature under dry sliding conditions using $Al_2O_3$ ball by employing a ball-on-disc tribometer configuration. Post-mortem analysis of the worn surfaces showed that the $Ti_3SiC_2$ MAX phase exhibited intrinsic self-lubricating behaviour owing to the evolution of easy shearing graphitic carbon at the sliding surface. The addition of TiC delayed the oxidation kinetics of $Ti_3SiC_2$ which favours the evolution of graphitic carbon in lieu of rutile and oxycarbide films. Thus, this work shows comprehensively the existence of intrinsic self-lubricating behaviour of $Ti_3SiC_2$ and the important role of the secondary phase TiC in the $Ti_3SiC_2$ matrix in its tribological behaviour. The wear mechanisms in both composites are dominated by tribo-oxidation triggered by frictional heating. This is then followed by deformation induced wear upon friction transition.

**Keywords:** MAX phases; Dry Sliding Friction; Frictional Heating; Tribofilm

## 1. INTRODUCTION

The $M_{n+1}AX_n$ phases are metallo-ceramics and they are comprised of an early transition metal M, an A – group (III, IV, V, or VI) element, X is C or N, and n ranges from 1 to 6 [1-5]. These ternary compounds are of interest because of their intercalated hexagonal near closed-packed

crystal structure, which forms nanolaminated layered structures [6, 7] that impart remarkable properties [8]. Figure 1 shows the unit cells of typical MAX phases for n = 1, n = 2, and n = 3, thus forming the so-called "312", "211", and "413" phase structures, owing to the stoichiometric ratio of the constituent elements.

These phases are important for several reasons:

1. They exhibit simultaneously ceramic and metallic characteristics [9, 10].
2. They possess crystal structure comparable to well-known solid lubricants like graphite and $MoS_2$ [11].
3. They deform by confining damage to a limited plastically deformed area by combining a range of energy absorbing mechanisms involving grain buckling, kink-band formation, and delamination of individual grains [12, 13]. This occurs despite them lacking the five independent slip systems necessary for classic metal ductility [9].
4. They are relatively soft (i.e., hardness ≈ 2 – 8 GPa) for a transition metal carbide, light (i.e., density ≈ 4.5 g/cm$^3$) and readily machineable like graphite [9].
5. High fracture toughness (7 – 9 MPa.m$^{1/2}$) [14].
6. They are damage tolerant, thermal shock resistant, and some are oxidation resistant up to 1400 °C (Al-containing MAX phases ($Ti_2AlC$, $Ta_2AlC$ and $Cr_2AlC$) [15-18], and some possess autonomous self-healing properties at high temperature (e.g., $Ti_2AlC$) [16, 17, 19-21].

These properties have led to increasing interest in MAX phases for potential structural applications, nuclear, tribological and high-temperature systems [7, 12, 22]. MAX phases possess a hexagonal crystal structure similar to graphite and previous studies indicate lubricating properties. Therefore, MAX phases have been speculated as candidates in a range of tribological applications [9, 23]. These applications include (i) electrical contacts, in the case

of Cu-MAX phase and Ag-MAX phase composite systems [24], (ii) applications in high-temperature gas-cooled reactors (HTRs) [25], and (iii) self-acting foil bearing rings in turbomachinery based systems [7].

In a previous work by Souchet et al. [26] on fine grained and coarse grained $Ti_3SiC_2$ sliding against $Si_3N_4$ they observed two successive regimes. In regime I, both coefficient of friction μ and wear rate were low. In regime II, followed, μ increased to a range of 0.4 to 0.5 whilst the wear rate became significant. Sakar et al. [27] studied the fretting wear of $Ti_3SiC_2$ against steel and concluded that the dominant wear mechanisms were abrasion, tribochemical layer formation and plastic deformation. Barsoum et al. [7] stated that the tribological behaviour of MAX phases are governed by complex tribochemistries, thus different tribolayers evolve with architectures dependent on the degree of oxidation as well as the mechanical properties such as adhesion to substrate and hardness. They classified tribofilms based on the triboreactions' source into four categories [7]: Type I if triboreaction occurs mainly at the MAX phase surface; Type II if triboreaction occurs at the countersurface; Type III if both the MAX phase and composite phase alongside the countersurface contribute to the tribofilm formation; and Type IV if the MAX-composite contributes predominantly to the tribofilm formation.

Recent work on the tribology of $Ti_3SiC_2$ is focused on reinforcing the $Ti_3SiC_2$ matrix by incorporating metal and/or ceramic particles to improve its tribological behaviour. Dang et al. [28] studied the tribological behaviour of $Cu/Ti_3SiC_2$ in comparison to monolithic $Ti_3SiC_2$. They reported that the tribological behaviour of $Cu/Ti_3SiC_2$ was superior to $Ti_3SiC_2$ owing to the formation of hard decomposition products ($TiC_X$, $Ti_5Si_3C_y$, $TiSi_2C_Z$, and $Cu_3Si$) during synthesis which inhibit abrasive friction and wear. Dang et al. [29] also reported on the tribological behaviour of $Ti_3SiC_2$/Cu/Al/SiC at elevated temperature, showing that the tribological behaviour of $Ti_3SiC_2$/Cu/Al/SiC MAX phase composite is better than that of monolithic $Ti_3SiC_2$ between room temperature and 200 °C. At higher temperatures the wear

properties of the composite were not better than monolithic $Ti_3SiC_2$. However, the incorporated phases in the $Ti_3SiC_2$ matrix reinforced the bonding of the $Ti_3SiC_2$ grains by pinning the surrounding soft $Ti_3SiC_2$ matrix under the cyclic stress. Yang et al. [30] studied the dry sliding friction and wear properties of $(TiB_2 + TiC)/Ti_3SiC_2$ and $TiC/Ti_3SiC_2$ composites against steel balls with load variation from 10 to 30 N. The composite $TiC/Ti_3SiC_2$ exhibited an increase in friction with increasing load whilst the friction coefficient of the $(TiB_2 + TiC)/Ti_3SiC_2$ was not sensitive to load. Furthermore, friction and wear rate of the $(TiB_2 + TiC)/Ti_3SiC_2$ composite was reported to be lower than that of $TiC/Ti_3SiC_2$ and this was solely attributed to the pinning effect of the hard $TiB_2$ and TiC particles on the soft $Ti_3SiC_2$ surrounding matrix, which helps to decentralize the shear stresses under the sliding ball.

An important potential application of MAX phases is in aerofoil bearing systems where intrinsic lubricity as well as low μs and WRs are required to mitigate friction and wear during engine start-up and shut-downs [31]. Also, owing to the low bearing load capacity of current aerofoil bearings, MAX phase composites consisting of second phase hard particles can be employed. Such a tribosystem would often incorporate Ni-based superalloys as counterface material. However, in this work alumina ($Al_2O_3$) was chosen because it is chemically inert and enables characterizing essentially the intrinsic lubricity of $Ti_3SiC_2$.

The scope of this work was to synthesize fully dense bulk $Ti_3SiC_2$ and $Ti_3SiC_2$-TiC samples via the Maxthal 312 and TiC powder route using spark plasma sintering (SPS) in order to establish the existence of intrinsic self-lubricity in $Ti_3SiC_2$ and to further evaluate them as possible triboactive materials for prospective aerofoil bearing tribological applications through detailed analysis of the worn surfaces. Furthermore, the role of $TiC_X$ formed in situ during the synthesis as well as the added TiC in the $Ti_3SiC_2$ soft matrix will be further explored. It is noteworthy to mention that the initial starting compositions obtained for tribological

investigation contained the ancillary phase $TiC_X$ owing to the starting composition of the Maxthal 312 prealloyed powder as well as reaction mechanisms explained elsewhere [32]. The powder synthesis and consolidation was carried out using spark plasma sintering (SPS) because it is an inexpensive powder metallurgy process owing to relatively short sintering times. SPS has unique sintering capabilities that incorporate simultaneously ON – OFF pulse DC electric current via joule heating, temperature and pressure during powder consolidation [33]. The ON – OFF electric current further enables localized high temperature to be transferred and dispersed at fine local areas between powder particles which reduces the sintering time [34]. Furthermore, the range of controllability of processing parameters (heating rate, load application rate, cooling rate, holding rate, etc.) makes SPS an extremely versatile process, as microstructures can be easily tailored in comparison to other conventional sintering techniques [35].

## 2. EXPERIMENTAL DETAILS

### *2.1. Materials and sample preparation*

Commercially available MAX phase pre-reacted powder Maxthal 312™ (nominally-$Ti_3SiC_2$) with particle size 2.5 µm and composition 92 wt.% $Ti_3SiC_2$ and 8 wt.% $TiC_X$ as ancillary phase as well as TiC powder (99.5 %, 2 µm particle size) were used as starting powders. To synthesize $Ti_3SiC_2$-TiC, 3 g of TiC powder was added to 12 g of Maxthal 312 powder, dry ball-milled continuously for 24 hours, and then sieved using a 200-mesh sieve. The powder particle size of the resulting Maxthal 312-TiC powder was about ~ 3.2 µm). The Maxthal 312 powder and the resulting Maxthal 312-TiC powder were then synthesized separately using spark plasma sintering (SPS) to produce bulk sample discs of Maxthal 312 and Maxthal 312-TiC, respectively. During SPS, the sintering parameters were: 1450 °C sintering temperature, hold time 10 min, sintering pressure 54 Mpa (≈ 16 kN), and sintering environment was vacuum (5

x $10^{-2}$ mbar). Next, disc surfaces were ground with SiC paper and polished down with a diamond paste of 0.25 micron to ensure the complete removal of the carburized surface.

### *2.2. Vickers Hardness and Density*

The density of the samples was measured using the Archimedes method according to the ASTM standard B962-13 [36], and relative density was calculated upon considering the various phases formed in the bulk samples using the mixture rule. Hardness measurements were done using a Vickers microhardness tester with an indentation load of 4.9 N for 10 sec. Five measurements were taken and their mean value reported. Separately, to further reveal the role of Vickers induced damage on the deformation microstructures of the synthesized discs, higher indentation load (49 N) was employed and the resulting Vickers damage characterized.

### *2.3. Tribological Test*

Dry sliding RT tests (25 °C / 29 % RH) were carried out using a ball on disc configuration with alumina ($Al_2O_3$ – 2 mm ball) employed as counterface material. The mean surface roughness of the ball and disc were measured using a stylus profilometer. The mean surface roughness (Ra) of the ball was 0.01µm, and the roughness of the disc after polishing was 0.06 µm. Tribological tests were conducted using a normal load of 0.5 N (~ 180 MPa Hertzian contact pressure), and rotational speeds of 50 and 100 rpm (corresponding to a sliding speed of 16 mm/sec, and 37 mm/sec, respectively) for a total sliding time of 60 min. The coefficient of friction was automatically measured and recorded in real time by the friction tester's computer system. The wear rate was determined by measuring the worn area from profilometric scans across the wear scars and the average worn area input in the tribometer's software to determine the wear rate.

### *2.4. Analysis*

The crystal structure of the SPS bulk Maxthal 312 and Maxthal 312-TiC samples were analyzed with X-ray diffractometer using Cu Kα radiation. The diffractogram were recorded in the 2Θ range 10 to 80° with a step size 0.02°. The morphologies of the pristine material and wear tracks were analysed using scanning electron microscopy as well as optical microscopy. The ball surfaces after sliding against the discs were also analysed using optical microscopy. The surface chemistries of the wear tracks were investigated using Raman spectroscopy and EDX analysis in the SEM.

## 3. RESULTS AND DISCUSSION

### *3.1. Phase Composition, Properties and Microstructure*

Figure 2 shows the XRD patterns of the synthesized SPSed discs. As shown the main phases are $Ti_3SiC_2$ and TiC and some small amount of $TiSi_2$ also coexists. The increase in TiC after SPS, especially in the Maxthal 312 bulk sample, is possibly linked to the carburization of $Ti_3SiC_2$ owing to the graphite rich environment stemming from the graphite tooling employed (i.e., graphite paper, dies and punches) and/or intrinsic decomposition at high sintering temperature [37]. The evolution of the $TiSi_2$ phase occurred because it is the compulsory intermediary phase necessary for the formation of $Ti_3SiC_2$ and has not been fully consumed during the synthesis [38].

In order to determine the phase content, the integrated calibration for a two-phase $Ti_3SiC_2$-TiC was employed, consistent with other previous work [39]. However, it is important to mention that Rietveld refinement phase analysis could not be employed, as the $Ti_3SiC_2$ appeared to have been textured preferentially in the pressing direction during the SPS synthesis leading to exaggerated intensity. Since the amount of $TiSi_2$ phase is relatively small, we can sensibly make an approximation by ignoring that phase and perform intensity calibration based on the work by Zhang et al. [39] thus:

$$W_{TSC} = \frac{1.80}{1.80+I_{TC}/I_{TSC}} \text{ and } W_{TSC} = \frac{I_{TC}/I_{TSC}}{1.80+I_{TC}/I_{TSC}}$$

Where $W_{TSC}$ and $W_{TC}$ represent the relative weight percentages of $Ti_3SiC_2$ and TiC, respectively, whilst $I_{TSC}$ and $I_{TC}$ are the main peak intensities of the $Ti_3SiC_2$ (104) and TiC (200), respectively.

Using the above relation the phase content for the Maxthal 312 sample was 76 wt.% $Ti_3SiC_2$ and 24 wt.% $TiC_X$ whilst for the Maxthal 312-TiC sample, the phase content was 61 wt.% $Ti_3SiC_2$ and 39 wt.% ($TiC_X$ + TiC). The phase composition shows that non-stoichiometric $TiC_X$ (x = 0.67 as indicated by phase identification software) and not stoichiometric TiC forms in situ during the synthesis of both the Maxthal 312 and Maxthal 312-TiC samples owing to possible decomposition and/or compositional phase shift according to the Ti-Si-C phase diagram, linked to silicon evaporation during the synthesis [37, 40]. During the synthesis of the Maxthal 312-TiC, formation occurs of both $TiC_X$ owing to in situ decomposition (as observed in the Maxthal 312 sample) and TiC due to TiC powder addition. The main difference between stoichiometric TiC and non-stoichiometric $TiC_X$ is that TiC possesses a higher density and hardness, superior oxidation resistance and possibly higher fracture toughness than $TiC_X$ [41]. These may as a consequence lead to differences in tribological behaviour of the $TiC_X$ in the Maxthal 312 disc phase composition and ($TiC_X$ + TiC) in the Maxthal 312-TiC disc phase composition.

Table 1 shows the densities and Vickers hardnesses of the SPSed Maxthal and composite samples. The theoretical densities of the samples are higher than the intrinsic density of $Ti_3SiC_2$ (4.52 g/cm$^3$) which can be linked to the evolution of the $TiC_X$ and the addition of TiC phases with density (4.92 g/cm$^3$). In general the samples were fully dense with relative density equalling 98 % for the Maxthal 312 sample and 99 % for the Maxthal 312-TiC sample,

respectively. The Vickers hardness of the samples were also higher than the intrinsic hardness of $Ti_3SiC_2$ (4 – 5 GPa) [10] mainly due to the increase in second phases in the matrix.

Backscattered electron images of the polished unetched synthesized compacts are shown in Figures 3 and 4. As shown the bright phases are the $Ti_3SiC_2$ phase and the dark phases are the $TiC_X$ and/or TiC phase whilst some small pockets of $TiSi_2$ (white arrow) coexist, consistent with the XRD phase analysis. The microstructures of both Maxthal 312 and Maxthal 312-TiC exhibited a duplex microstructure where large grains are surrounded by a mixture of small grains (Figures 3b and 4b).

## 4. TRIBOLOGICAL PROPERTIES

### *4.1. Friction Evolution and Wear*

Figure 5 shows the evolution of the friction coefficient of the discs against the $Al_2O_3$ ceramic ball at room temperature. As shown in Fig. 5, the lowest friction coefficient was obtained from the Maxthal 312 -TiC disc (~ 0.2) for the test condition 50 rpm for 60 min. The friction curve was very stable and no fluctuation was observed. The mean friction coefficient for the Maxthal 312-TiC disc for the test condition 100 rpm for 60 min was around ~ 0.38 exhibiting a transition in friction from a stable low friction regime to an unstable high friction regime. On the other hand, for the Maxthal 312 disc with test condition 50 rpm for 60 min, the friction coefficient was initially very low (~ 0.15 – 0.25) and stable and subsequently underwent a transition to an unstable high friction coefficient regime. The Maxthal 312 disc with test condition 100 rpm for 60 min, meanwhile, initially had a low friction coefficient (0.2 – 0.4) for a very short time as compared to other samples and was followed by a transition to a high friction regime (~ 0.9). The reason for the fluctuations in friction coefficient following the transition is not fully understood; however, the role of tribofilm and/or wear debris generation cannot be ruled out.

Figure 6 shows the wear rates of the disc samples against the $Al_2O_3$ ceramic ball for the test conditions. The wear rate of the Maxthal 312-TiC disc for the contact conditions 0.5 N / 50 rpm / 60 min and 0.5 N / 100 rpm / 60 min were 2.06 x $10^{-7}$ $mm^3$/(Nm) and 1.26 x $10^{-6}$ $mm^3$/(Nm), respectively. For the Maxthal 312 disc, the wear rate for the contact test conditions 0.5 N / 50 rpm / 60 min and 0.5 N / 100 rpm / 60 min were 2.93 x $10^{-5}$ $mm^3$/(Nm) and 9.63 x $10^{-5}$ $mm^3$/(Nm), respectively. The increase in TiC content in the Maxthal 312-TiC appears to play a major role on the friction and wear behaviour of $Ti_3SiC_2$.

### *4.2. Worn Surface Chemistry*

#### *4.2.1. EDX Analysis*

Figure 7 shows the EDX compositional mapping of an area of the worn surface of the Maxthal 312 disc for the test condition 100 rpm / 60 min. The presence of oxygen in the wear track indicates an oxidation phenomenon possibly due to frictional heating owing to the dry sliding test condition. The Si-rich area appears to be depleted of oxygen and titanium whilst the Ti-rich region appears to have been preferentially oxidized in lieu of Si to form possibly rutile ($TiO_2$). The absence of Al in the wear track implied no transfer of material from the ball into the sliding surface took place during the test. The wear track also appeared to be rich in carbon, however it is not possible using EDX analysis to separate the evolution of a graphitic layer during wear from the intrinsic carbon in the MAX phase composition.

The EDX compositional map acquired from the worn surface of the Maxthal 312-TiC disc (Figure 8) for the test condition 100 rpm / 60 min showed that beside the evolution of oxygen consistent with chemistry of the worn surface of the Maxthal 312 disc, Al coexisted in the worn surface. The presence of Al may be directly linked to the presence of TiC in addition to the $TiC_X$ in the Maxthal 312-TiC bulk sample. Also, the oxygen content in the wear track of the

Maxthal 312-TiC is much more significant than that observed in the wear track of Maxthal 312.

### *4.2.2. Raman Analysis*

In order to further understand the chemistry inside wear tracks of the sliding surfaces of the Maxthal 312 and Maxthal 312-TiC discs, Raman analysis was carried out to supplement the EDX analysis. Raman analysis of the Maxthal 312 disc sliding surface (Figure 9) revealed the presence of rutile ($TiO_2$), titanium oxycarbide ($TiC_XO_Y$), and graphitic carbon, respectively. As the sliding speed is increased from 50 to 100 rpm the rutile and oxycarbide tribofilms tend to grow whilst the graphitic layer remains unchanged with sliding speed.

Raman analysis of the Maxthal 312-TiC sliding surface (Figure 10) revealed that at 50 rpm the tribofilm at the sliding surface was essentially graphitic carbon. However, as the sliding speed is increased to 100 rpm the evolution of rutile and oxycarbide can be seen whilst the graphitic layer grows with increased sliding speed. It appears that the incorporation of TiC into the $Ti_3SiC_2$ matrix slows down its oxidation kinetics as compared to the presence of in situ formed $TiC_X$ in the matrix. This observation is in agreement with EDX analysis as the higher oxygen content in the Maxthal 312-TiC sliding surface implied it formed later as compared to Maxthal 312 where the tribofilm formation occurred earlier and has been subsequently worn off.

## *4.3. Alumina Ball Analysis*

Figures 11 and 12 show the sliding surface of the $Al_2O_3$ pin after dry sliding against the Maxthal 312 and Maxthal 312-TiC discs for the contact conditions 50 rpm for 60 min (Figure 11) and 100 rpm for 60 min (Figure 12), respectively. For the test run at 50 rpm for 60 min, the $Al_2O_3$ pin surface after sliding against the Maxthal 312 disc appeared to have been slightly damaged and rough with some transfer film alongside with large amount of wear debris evident. On the

other hand, the $Al_2O_3$ pin surface after dry sliding against Maxthal 312-TiC appeared to be relatively smooth with some transfer film and slight scratches evident on is surface.

For the contact condition 100 rpm for 60 min, increased wear debris and transfer layer can be observed on the pins' surface after sliding against the Maxthal 312 and Maxthal 312-TiC discs. In addition, the surface of the $Al_2O_3$ pins appeared to have been fractured with severe wear grooves evident on the pin surface after sliding against the Maxthal 312 disc especially. It is noteworthy to further mention that the lack of elemental Al in the wear track of Maxthal 312/$Al_2O_3$ seen in EDX analysis (Figure 7) is surprising owing to the severity of the $Al_2O_3$ worn surface.

### *4.4. Worn Surface SEM Analysis*

Post-mortem analyses of the worn surfaces of the discs were carried out using SEM to analyse the sliding surfaces pre- and post-transition. Short friction tests were carried out on the Maxthal 312 and Maxthal 312-TiC discs and terminated just before the transition in friction (Figure 5) to produce pre-transition wear surfaces and the resulting SEM micrographs of the sliding surfaces are shown in Figure 13a and 13b. As revealed by SEM, the pre-transition sliding surfaces of the Maxthal 312 and Maxthal 312-TiC discs consist of mainly tribofilms with little or no damage at the sliding surfaces.

Analysis of the sliding surfaces of the Maxthal 312 and Maxthal 312-TiC discs post-transition for the entire test duration and contact conditions (Figures 14 and 15) showed extensive grain damage especially in the Maxthal 312 disc (Figure 14) sliding surface which is consistent with the friction evolution curve. It appears that the $Ti_3SiC_2$ grains in the Maxthal 312 can be easily pulled out owing to limited $TiC_X$ in the surrounding $Ti_3SiC_2$ matrix, as compared to the extensive pinning effect introduced by the ($TiC_X$ + TiC) on the $Ti_3SiC_2$ grains in the Maxthal 312-TiC sample, thus limiting pull-out of grains and shear deformation of $Ti_3SiC_2$ during

sliding contact, consistent with observations reported elsewhere [28-30]. It appears that the incorporation of TiC particles into the $Ti_3SiC_2$ matrix deteriorates its fracture toughness as pronounced lateral cracks at the indentation diagonals can be observed upon Vickers indentation on the Maxthal 312-TiC disc (Figure 16b). This is in contrast with the Maxthal 312 disc (Figure 16a) where little or no lateral cracking can be seen, owing to extensive deformation of the grains leading to severe grain pile-ups and push-outs around the indentation zone. It has been observed that these microscale energy absorbing mechanisms such as grain pile ups, grain push outs, grain buckling, kink band formation and eventual grain delamination are responsible for the signature damage tolerance observed in MAX phases [42]. The lack of significant deformation in the Maxthal 312-TiC other than cracking implies that the Maxthal 312-TiC sample is less prone to shear deformation by sliding as compared to the Maxthal 312 sample, owing to the extensive pinning effect introduced by the ($TiC_X$ and TiC) particles around the $Ti_3SiC_2$ grains thus inhibiting deformation.

## 5. FRICTION TRANSITION AND WEAR MECHANISMS

### *5.1. Friction Transition*

At the start of the experiment i.e., the pre-transition regime, easy shearing graphitic carbon forms at the sliding surface as found in the Raman data, thus the low coefficients of friction μ and the low wear rates in this regime as observed in Maxthal 312 and Maxthal 312-TiC discs. Over time, as found here by SEM-EDX and Raman analysis, $TiO_2$ and $TiC_XO_Y$ form at the sliding surface in addition to the graphitic carbon, possibly due to frictional heating. However, it appears that the $TiO_2$ and/or $TiC_XO_Y$ can be easily worn off the sliding surface possibly due to their brittle nature or spalled off upon reaching a critical thickness which then results in abrasive third body material (as evident owing to the wear grooves on the alumina ball surface); hence the transition in friction from low μ and the low wear rates to high μ and high wear rates

in regime II (post transition). The absence of a transition in friction as observed in the Maxthal 312-TiC/$Al_2O_3$ at 50 rpm is mainly due to little or no presence of the brittle $TiO_2$ and $TiC_XO_Y$ tribofilms as seen in the Raman data in Figure 10 that can be easily worn or spalled off at the sliding surface.

### *5.2. Wear Mechanisms*

The wear mechanisms (Figure 17) upon careful study of the chemistry and morphology of the wear tracks of the Maxthal 312 and Maxthal 312-TiC discs are summarized thus:

Tribo-oxidative wear (leading to transition)

Owing to the dry-sliding condition, frictional heating results in the oxidation of the sliding surface that brings about the evolution of $TiO_2$ and $TiC_XO_Y$, thus the transition in friction and onset of deleterious wear.

Deformation induced wear (post transition)

Upon transition in friction, direct contact between the $Al_2O_3$ ball and the discs is initiated which then results in microscale deformation (i.e., kink band formation and grain delamination), grain fracture, and eventual grain pull-outs at the sliding surface. As a result, third-body abrasive wear owing to the fracture and pull-outs of the $Ti_3SiC_2$ grains will dominate the wear mechanism.

## 6. CONCLUSIONS

The following salient conclusions have been reached upon exhaustive analysis of the pin and discs surfaces:

- $Ti_3SiC_2$ MAX phase is indeed intrinsically self-lubricating owing to the lubrication action of graphitic carbon essentially as well as titanium oxycarbide.

- The disruption in tribofilm architecture led to the transition in friction and wear owing to formation of titanium oxide and its subsequent spallation.
- TiC slows the oxidation kinetics of $Ti_3SiC_2$ thus favouring solely the presence of easy shearing graphitic carbon at the sliding surface.
- $Ti_3SiC_2$-TiC might be suitable for airfoil bearing systems due to the intrinsic self-lubricity and damage tolerance of $Ti_3SiC_2$ and the load bearing capability of the TiC second phase.

## REFERENCES


1. Hong Ng, V.M., et al., Recent progress in layered transition metal carbides and/or nitrides (MXenes) and their composites: synthesis and applications. Journal of Materials Chemistry A, 2017. **5**(7): p. 3039-3068.
2. Eklund, P., J. Rosen, and P.O.Å. Persson, Layered ternary Mn+1AXnphases and their 2D derivative MXene: an overview from a thin-film perspective. Journal of Physics D: Applied Physics, 2017. **50**(11): p. 113001.
3. Fashandi, H., et al., Ti2Au2C and Ti3Au2C2 formed by solid state reaction of gold with Ti2AlC and Ti3AlC2. Chemical Communications, 2017. **53**(69): p. 9554-9557.
4. Fashandi, H., et al., Synthesis of Ti3AuC2, Ti3Au2C2 and Ti3IrC2 by noble metal substitution reaction in Ti3SiC2 for high-temperature-stable Ohmic contacts to SiC. Nature Materials, 2017. **16**: p. 814.
5. Sokol, M., et al., Big Questions in Chemistry - On the Chemical Diversity of the MAX Phases. 2019.
6. Mo, Y., et al., Crystal Structure and Elastic Properties of Hypothesized MAX Phase-Like Compound (Cr2Hf)2Al3C3. Journal of the American Ceramic Society, 2014. **97**(8): p. 2646-2653.
7. Gupta, S. and M.W. Barsoum, On the tribology of the MAX phases and their composites during dry sliding: A review. Wear, 2011. **271**(9–10): p. 1878-1894.
8. Smialek, J.L., Oxidation of Al2O3 Scale-Forming MAX Phases in Turbine Environments. Metallurgical and Materials Transactions A, 2018. **49**(3): p. 782-792.
9. Barsoum, M.W., MAX phases : properties of machinable ternary carbides and nitrides. 2013: Weinheim, Germany : Wiley-VCH Verlag GmbH & Co. KGaA, 2013.
10. Barsoum, M.W. and M. Radovic, Elastic and Mechanical Properties of the MAX Phases, in Annual Review of Materials Research, Vol 41, D.R. Clarke and P. Fratzl, Editors. 2011, Annual Reviews: Palo Alto. p. 195-227.
11. Shi, X., et al., Friction and Wear Properties of TiAl-Ti3SiC2-MoS2 Composites Prepared by Spark Plasma Sintering AU - Zhai, Wenzheng. Tribology Transactions, 2014. **57**(3): p. 416-424.
12. Le Flem, M. and X.M. Liu, 14 - Stability of Ti3SiC2 under charged particle irradiation A2 - Low, I.M, in Advances in Science and Technology of Mn+1axn Phases. 2012, Woodhead Publishing. p. 355-387.
13. Barsoum, M.W., L. Farber, and T. El-Raghy, Dislocations, kink bands, and room-temperature plasticity of Ti3SiC2. Metallurgical and Materials Transactions A, 1999. **30**(7): p. 1727-1738.
14. Barsoum, M.W. and T. El-Raghy, Synthesis and Characterization of a Remarkable Ceramic: Ti3SiC2. Journal of the American Ceramic Society, 1996. **79**(7): p. 1953-1956.
15. Haftani, M., et al., Studying the oxidation of Ti2AlC MAX phase in atmosphere: A review. International Journal of Refractory Metals and Hard Materials, 2016. **61**: p. 51-60.
16. Kwakernaak, C. and W.G. Sloof, Work of adhesion of interfaces between M2AlC (M = Ti, V, Cr) MAX phases and α-Al2O3. Ceramics International, 2018. **44**(18): p. 23172-23179.
17. Shen, L., et al., Reducing the erosive wear rate of Cr2AlC MAX phase ceramic by oxidative healing of local impact damage. Wear, 2016. **358-359**: p. 1-6.
18. Farle, A.-S., et al., Oxidation and self-healing behaviour of spark plasma sintered Ta2AlC. Vol. 37. 2017.
19. Qian, X.K., 1 - Methods of MAX-phase synthesis and densification – I A2 - Low, I.M, in Advances in Science and Technology of Mn+1axn Phases. 2012, Woodhead Publishing. p. 1-19.
20. Sloof, W.G., et al., Repeated crack healing in MAX-phase ceramics revealed by 4D in situ synchrotron X-ray tomographic microscopy. Scientific Reports, 2016. **6**: p. 23040.
21. Farle, A.-S., et al., A conceptual study into the potential of Mn+1AXn-phase ceramics for self-healing of crack damage. Journal of the European Ceramic Society, 2015. **35**(1): p. 37-45.

22. Pang, W.K. and I.M. Low, 15 - Understanding and improving the thermal stability of layered ternary carbides in ceramic matrix composites, in Advances in Ceramic Matrix Composites, I.M. Low, Editor. 2014, Woodhead Publishing. p. 340-368.
23. Sun, Z.M., Progress in research and development on MAX phases: a family of layered ternary compounds. International Materials Reviews, 2011. **56**(3): p. 143-166.
24. Grieseler, R., et al., Copper-MAX-phase composite coatings obtained by electro-co-deposition: A promising material for electrical contacts. Surface and Coatings Technology, 2017. **321**: p. 219-228.
25. Zhu, Y., et al., Tribological Properties of Ti3SiC2 coupled with different counterfaces. Vol. 41. 2015.
26. Souchet, A., et al., Tribological duality of Ti3SiC2. Tribology Letters, 2005. **18**(3): p. 341-352.
27. Sarkar, D., B.V.M. Kumar, and B. Basu, Understanding the fretting wear of Ti3SiC2. Journal of the European Ceramic Society, 2006. **26**(13): p. 2441-2452.
28. Dang, W., et al., Influence of Cu on the mechanical and tribological properties of Ti3SiC2. Ceramics International, 2016. **42**(8): p. 9972-9980.
29. Dang, W., et al., The tribological properties of Ti3SiC2/Cu/Al/SiC composite at elevated temperatures. Tribology International, 2016. **104**: p. 294-302.
30. Yang, J., et al., Friction and wear properties of in situ (TiB2+TiC)/Ti3SiC2 composites. Wear, 2011. **271**(11): p. 2940-2946.
31. DellaCorte, C., A. R. Zaldana, and K. C. Radil, A Systems Approach to the Solid Lubrication of Foil Air Bearings for Oil-Free Turbomachinery. Vol. 126. 2002.
32. Magnus, C. and W.M. Rainforth, Influence of sintering environment on the spark plasma sintering of Maxthal 312 (nominally-Ti3SiC2) and the role of powder particle size on densification. Journal of Alloys and Compounds, 2019. **801**: p. 208-219.
33. Zhang, F., et al., The potential of rapid cooling spark plasma sintering for metallic materials. Materials Today, 2013. **16**(5): p. 192-197.
34. Tokita, M., Mechanism of spark plasma sintering. Vol. 21. 2001. 729-732.
35. Aalund, R., Spark Plasma Sintering. Issue of Ceramic Industry, 2008.
36. Powders, B.M. and P. Metal Powder, Standard Test Methods for Density of Compacted or Sintered Powder Metallurgy (PM) Products Using Archimedes' Principle. 2008.
37. El-Raghy, T. and M.W. Barsoum, Diffusion kinetics of the carburization and silicidation of Ti3SiC2. Journal of Applied Physics, 1998. **83**(1): p. 112-119.
38. Kero, I., R. Tegman, and M.-L. Antti, Phase reactions associated with the formation of Ti3SiC2 from TiC/Si powders. Ceramics International, 2011. **37**(7): p. 2615-2619.
39. Zhang, Z.F., Z.M. Sun, and H. Hashimoto, Rapid synthesis of ternary carbide Ti3SiC2 through pulse-discharge sintering technique from Ti/Si/TiC powders. Metallurgical and Materials Transactions A, 2002. **33**(11): p. 3321-3328.
40. Kero, I., R. Tegman, and M.-L. Antti, Effect of the amounts of silicon on the in situ synthesis of Ti3SiC2 based composites made from TiC/Si powder mixtures. Ceramics International, 2010. **36**(1): p. 375-379.
41. Zhang, Z., et al., Processing and mechanical properties of nonstoichiometric TiCx ($0.3 \leq x \leq 0.5$). Ceramics International, 2018. **44**(15): p. 18996-19001.
42. Li, S.B., L.F. Cheng, and L.T. Zhang, Identification of damage tolerance of Ti3SiC2 by hardness indentations and single edge notched beam test. Materials Science and Technology, 2002. **18**(2): p. 231-233.

**TABLES AND FIGURES**

Table 1. Density and Vickers hardness of the polished SPSed discs

| ***Disc samples*** | *Theoretical density* ($g/cm^3$) | *Measured density* ($g/cm^3$) | *Relative density* (%) | *Vickers hardness* (GPa) |
|---|---|---|---|---|
| ***Maxthal 312*** | *4.62* | *4.54* | *98* | *9.4* |
| ***Maxthal 312-TiC*** | *4.68* | *4.65* | *99* | *12.6* |

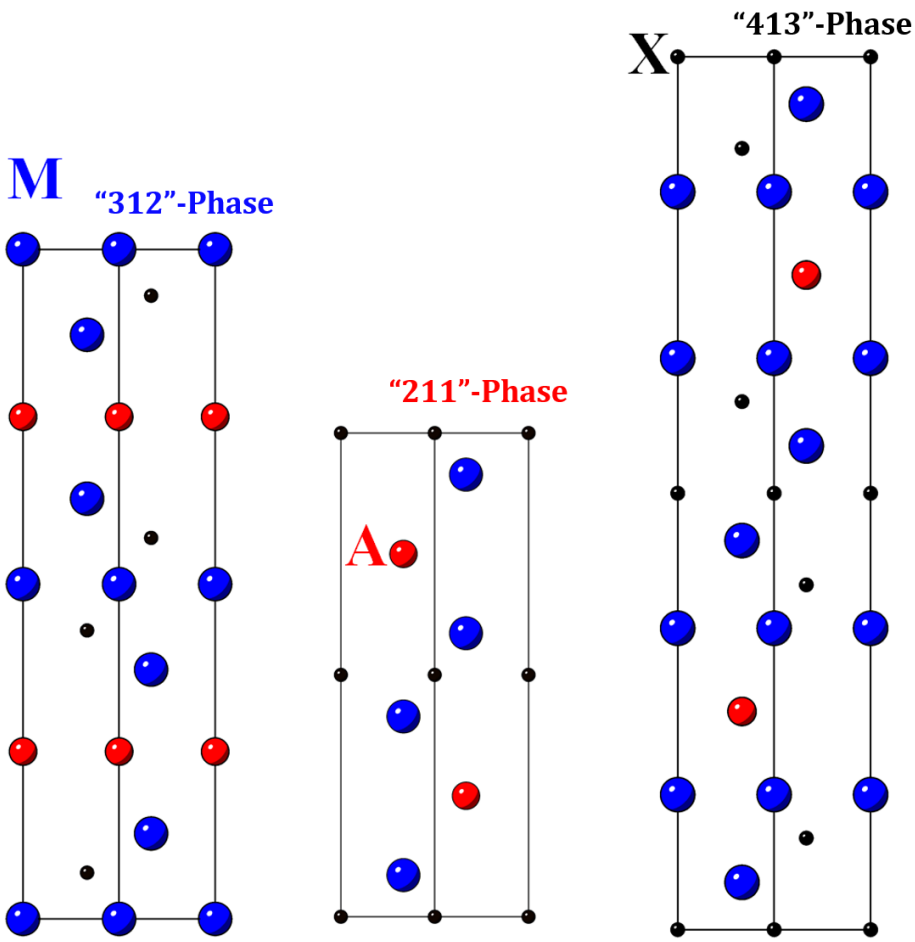


**Fig. 1.** Crystal structure of some MAX phase systems crystallizing in $P6_3/mmc$.

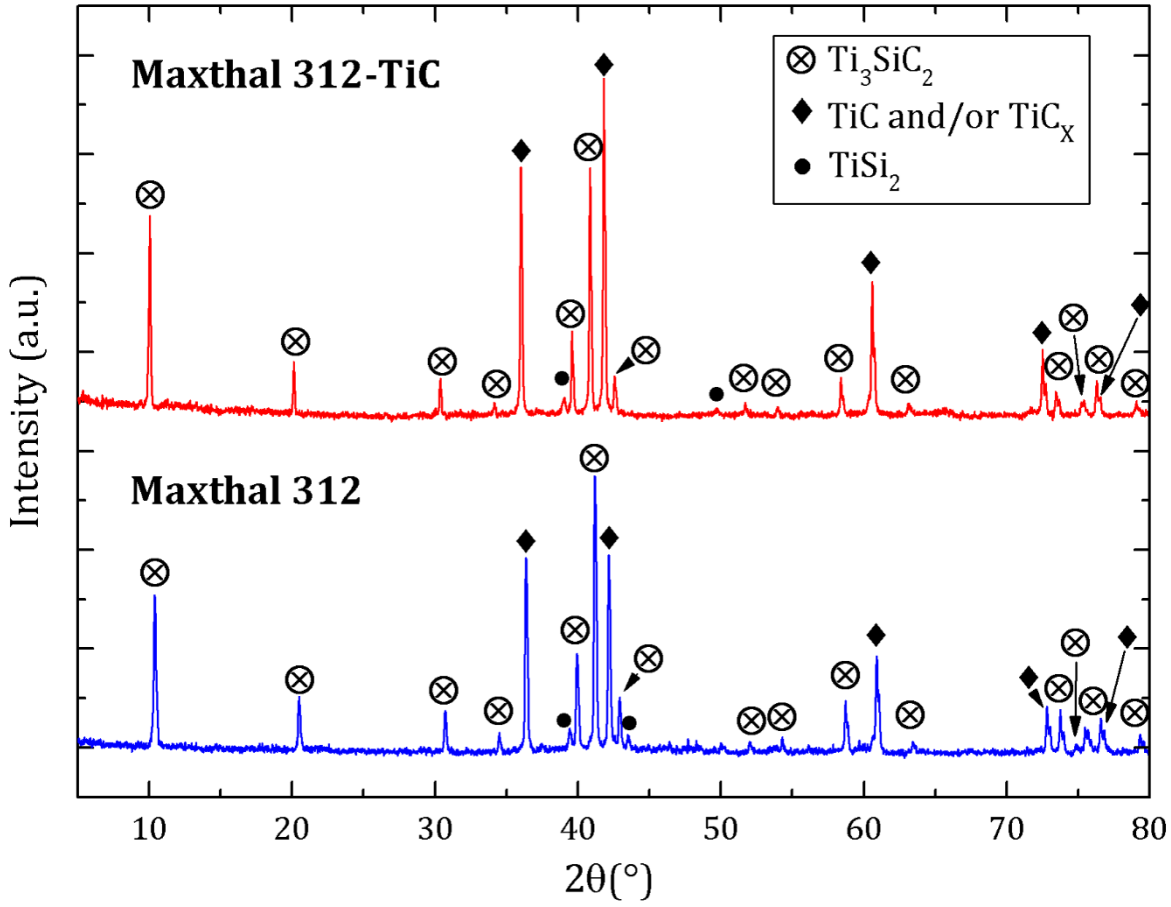


**Fig. 2.** XRD patterns of the synthesized Maxthal 312 and Maxthal 312-TiC polished bulk samples.

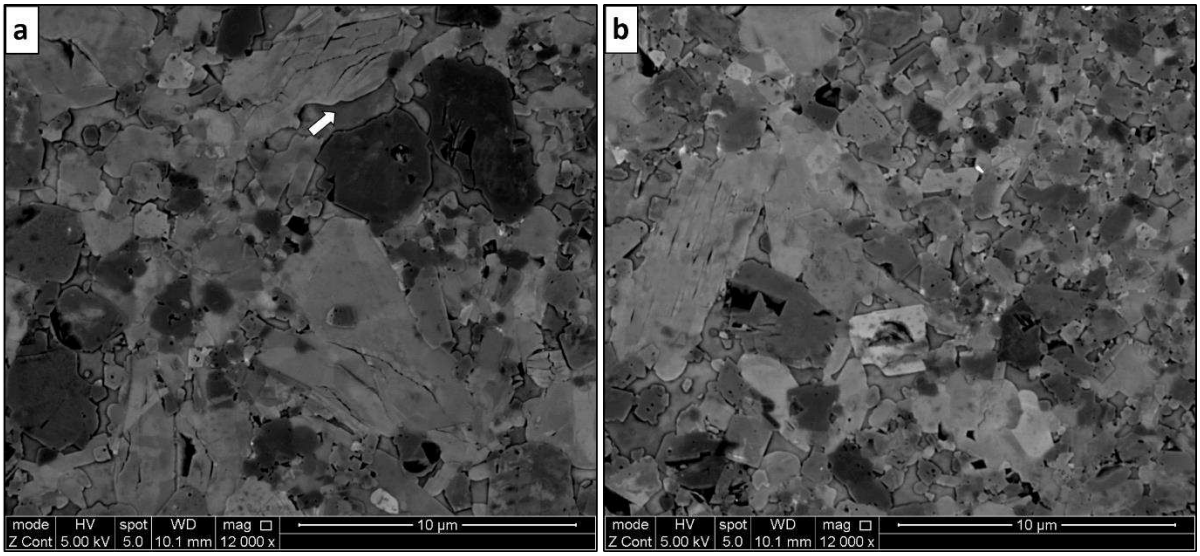


**Fig. 3.** Back scattered SEM micrographs of the bulk Maxthal 312 sample. Note: white arrow in (a) showing the silicide region as confirmed by EDX.

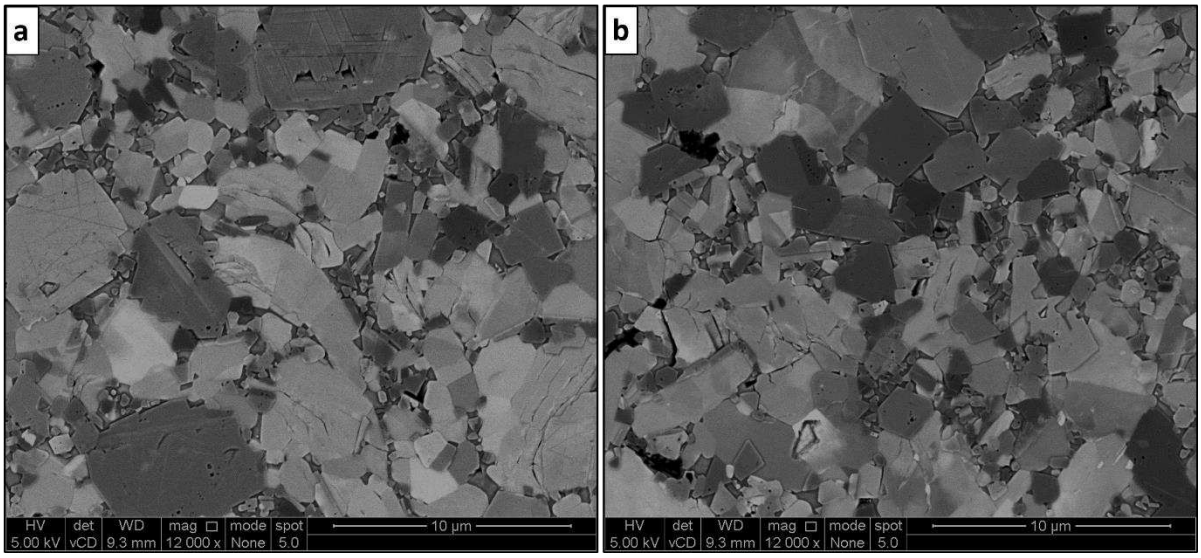


**Fig. 4.** Back scattered SEM micrographs of the bulk Maxthal 312-TiC sample.

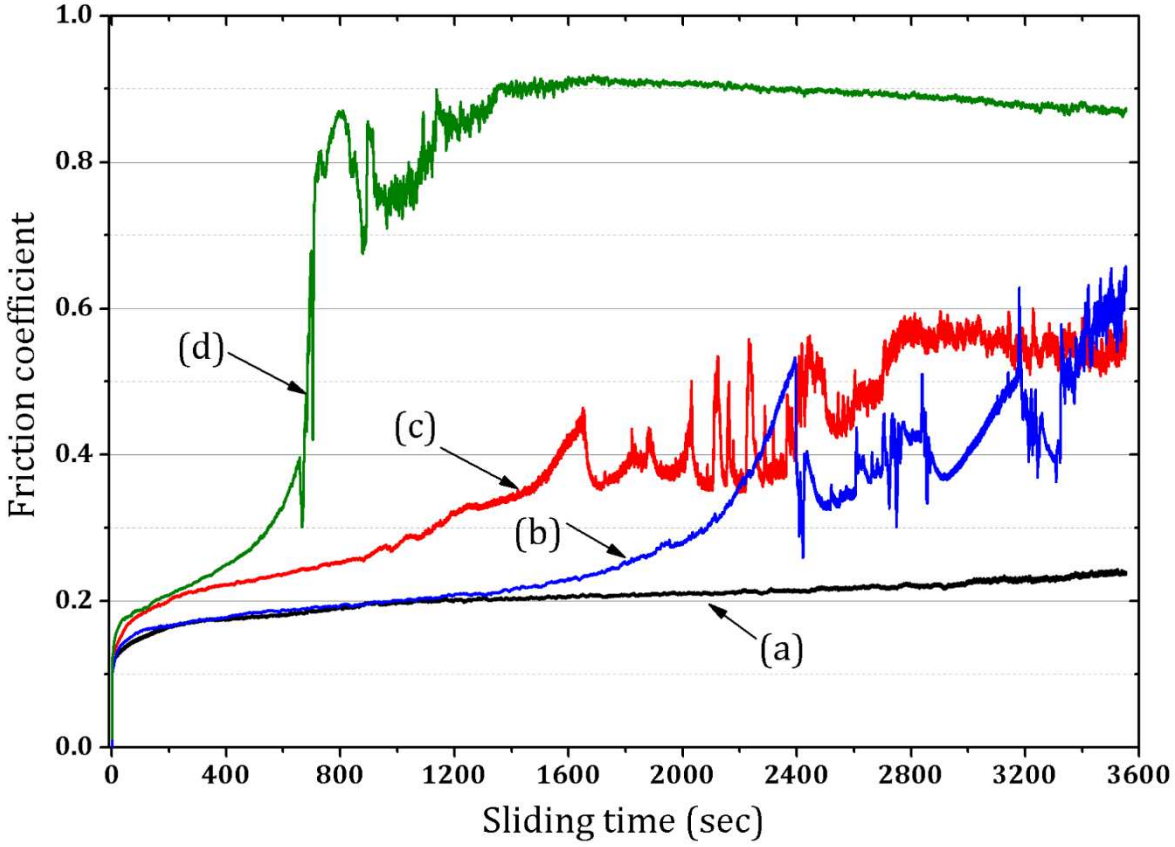


**Fig. 5.** The evolution of friction coefficients of the bulk samples upon sliding against $Al_2O_3$ ceramic using a constant normal load of 0.5 N: (a) Maxthal 312-TiC (50 rpm / 60 min), (b) Maxthal 312 (50 rpm / 60 min), (c) Maxthal 312-TiC (100 rpm / 60 min), and (d) Maxthal 312 (100 rpm / 60 min).

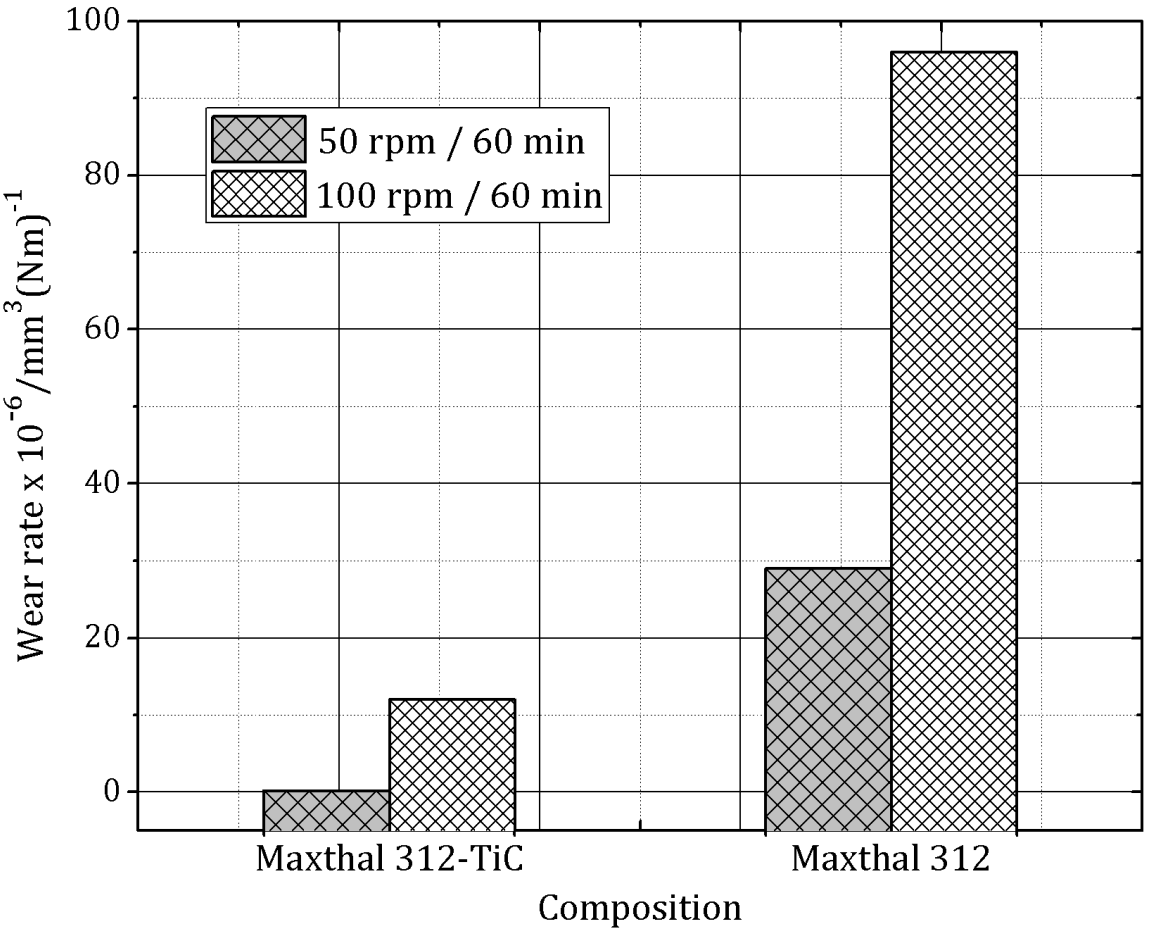


**Fig. 6.** The wear rates of the SPSed bulk samples upon sliding against $Al_2O_3$ ceramic ball at RT.

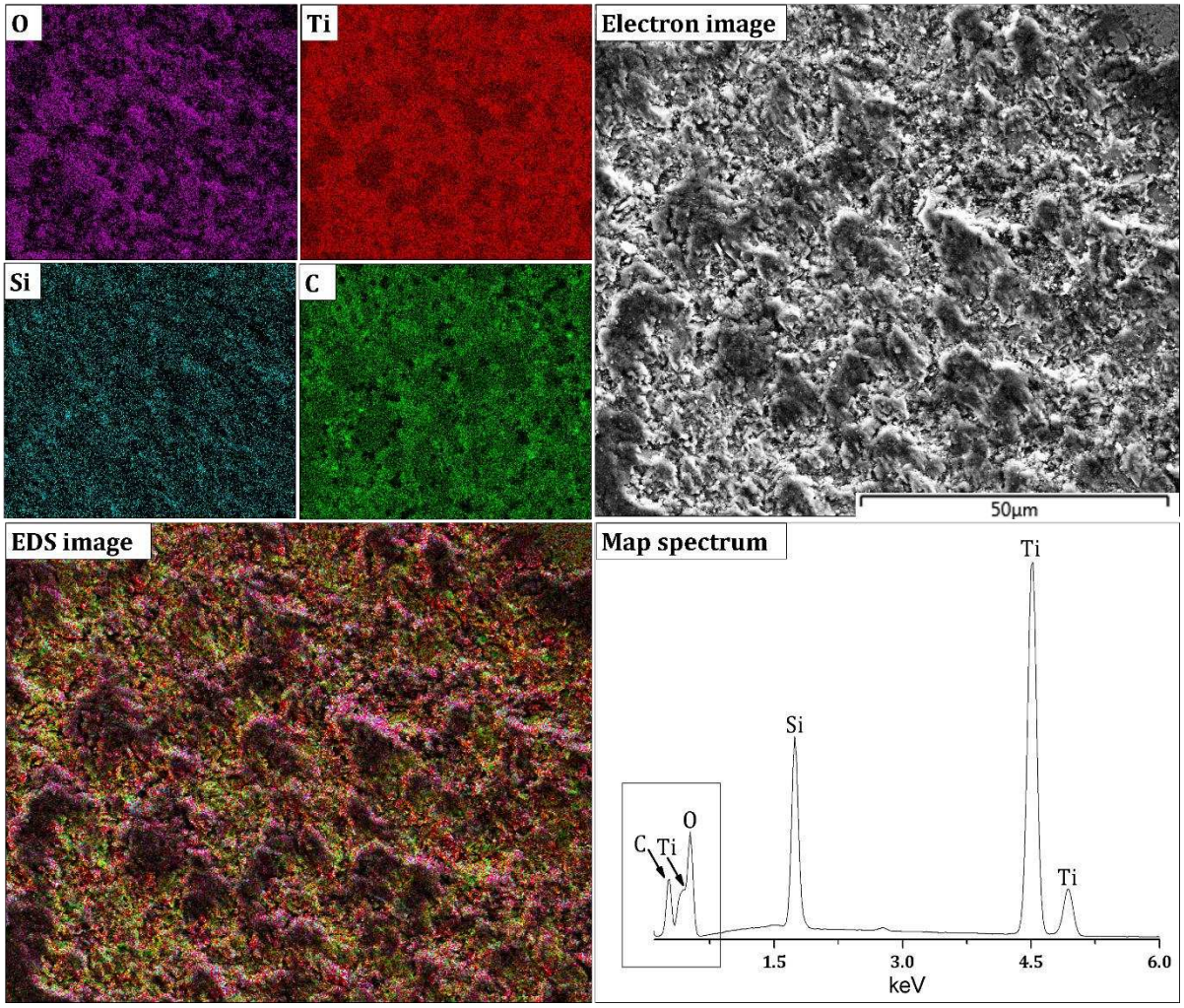


**Fig. 7.** EDX elemental distribution map and spectrum inside the wear track of the Maxthal 312/$Al_2O_3$ worn section from wear conditions 100 rpm / 60 min.

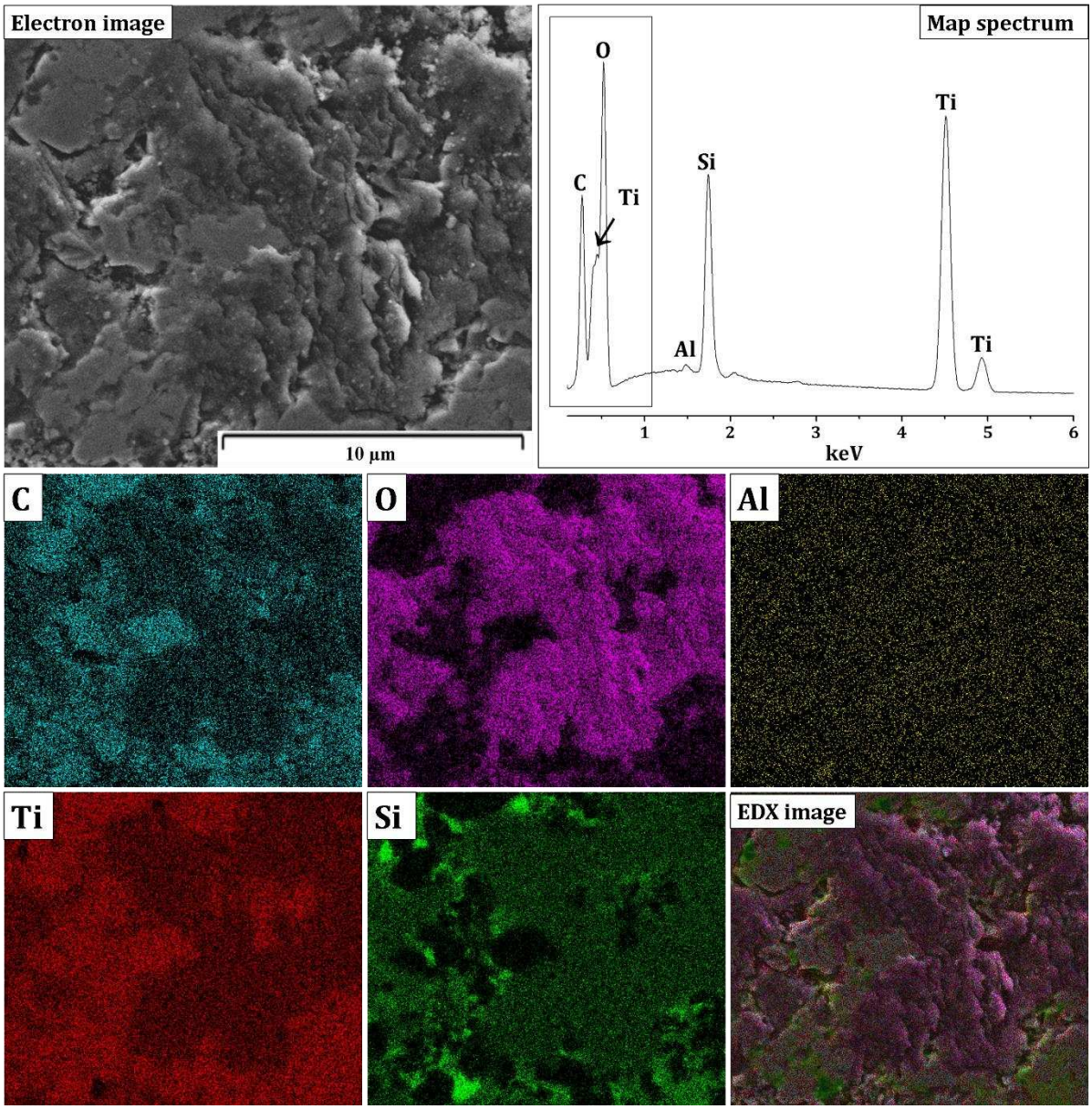


**Fig. 8.** EDX elemental distribution map and spectrum inside the wear track of Maxthal 312-TiC/$Al_2O_3$ worn section from wear condition 100 rpm / 60 min.

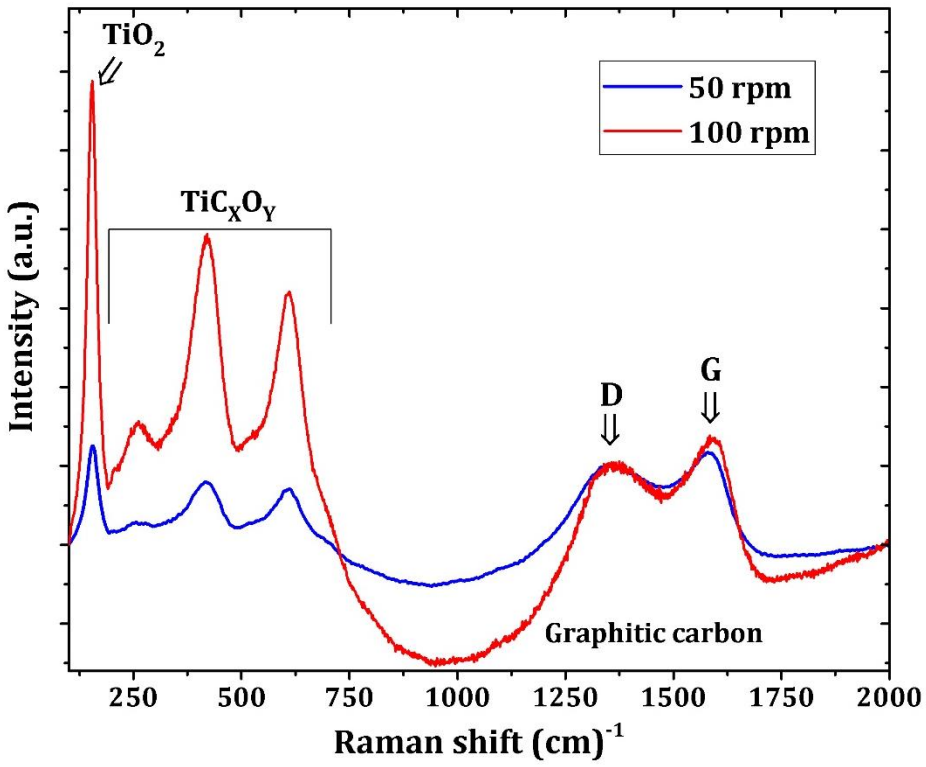


**Fig. 9.** Raman spectra acquired inside the wear track of the Maxthal 312/$Al_2O_3$ tribocouples.

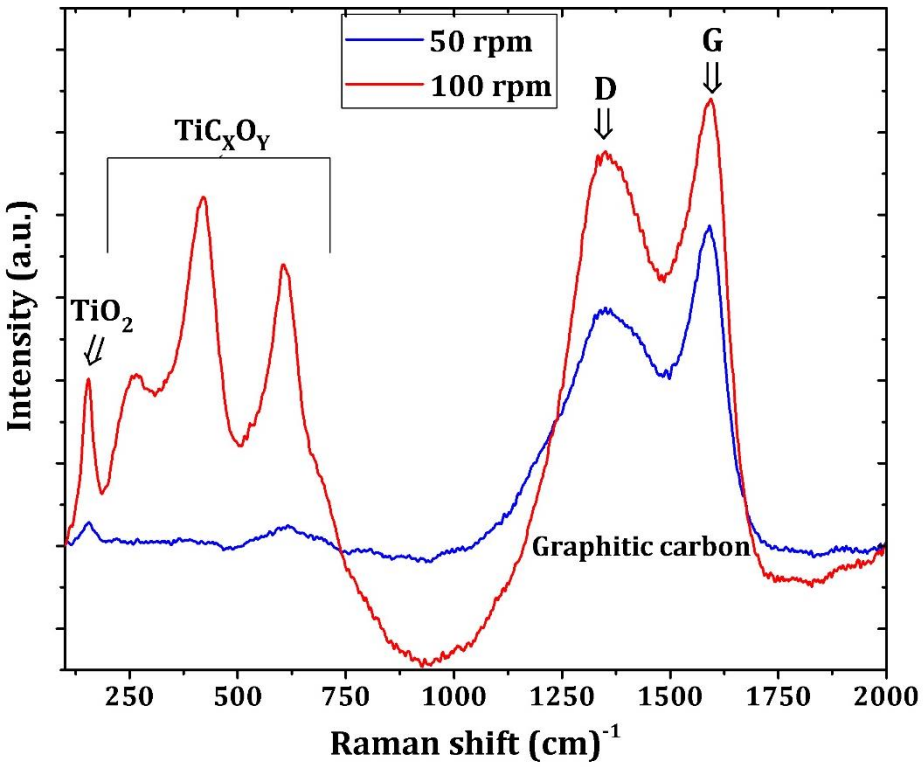


**Fig. 10.** Raman spectra acquired inside the wear track of the Maxthal 312-TiC/$Al_2O_3$ tribocouples.

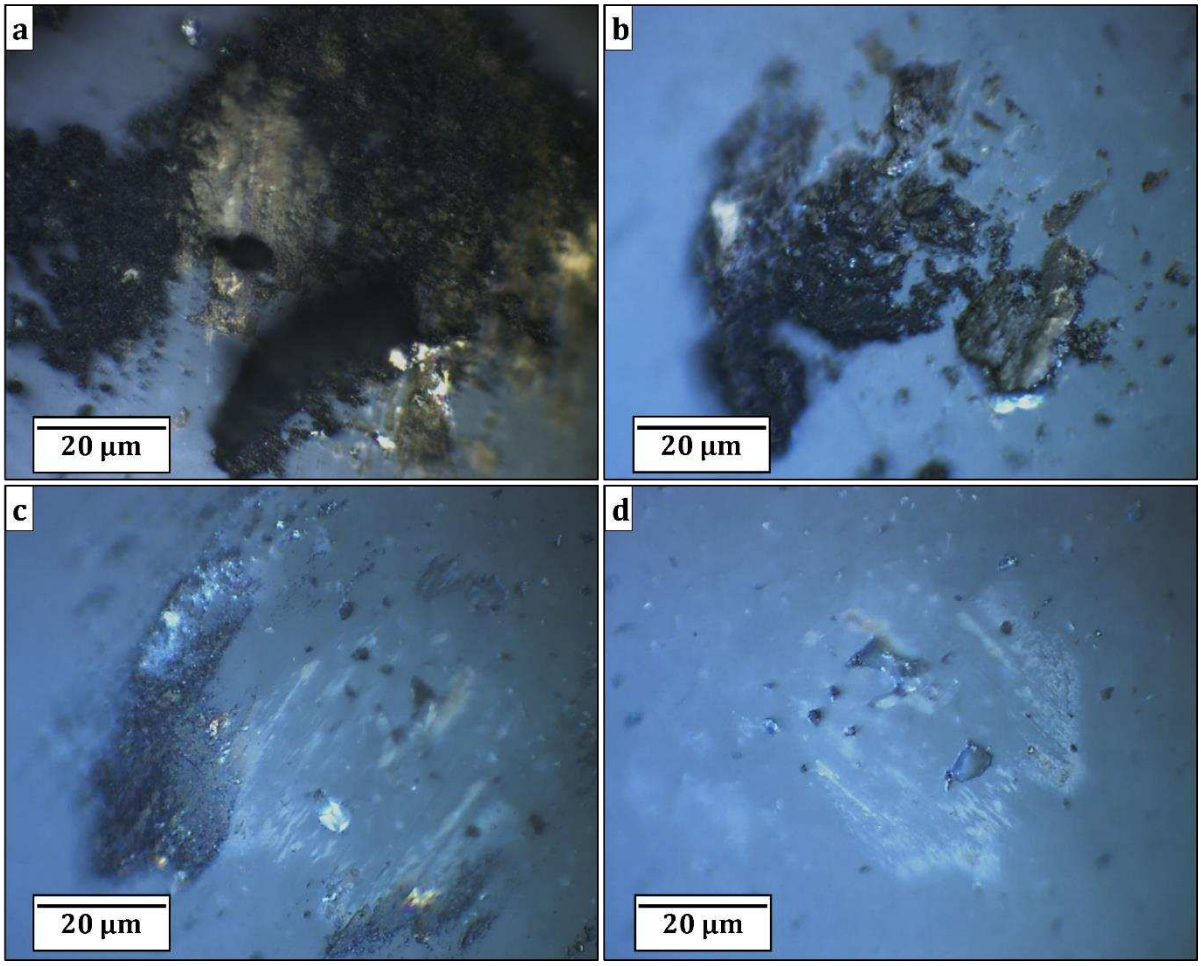


**Fig. 11**. Optical images of the $Al_2O_3$ ball surface after unlubricated sliding against the Maxthal 312 disc ((a) before cleaning and (b) after cleaning) and Maxthal 312-TiC disc ((c) before cleaning and (d) after cleaning) discs for the contact condition 50 rpm for 60 min.

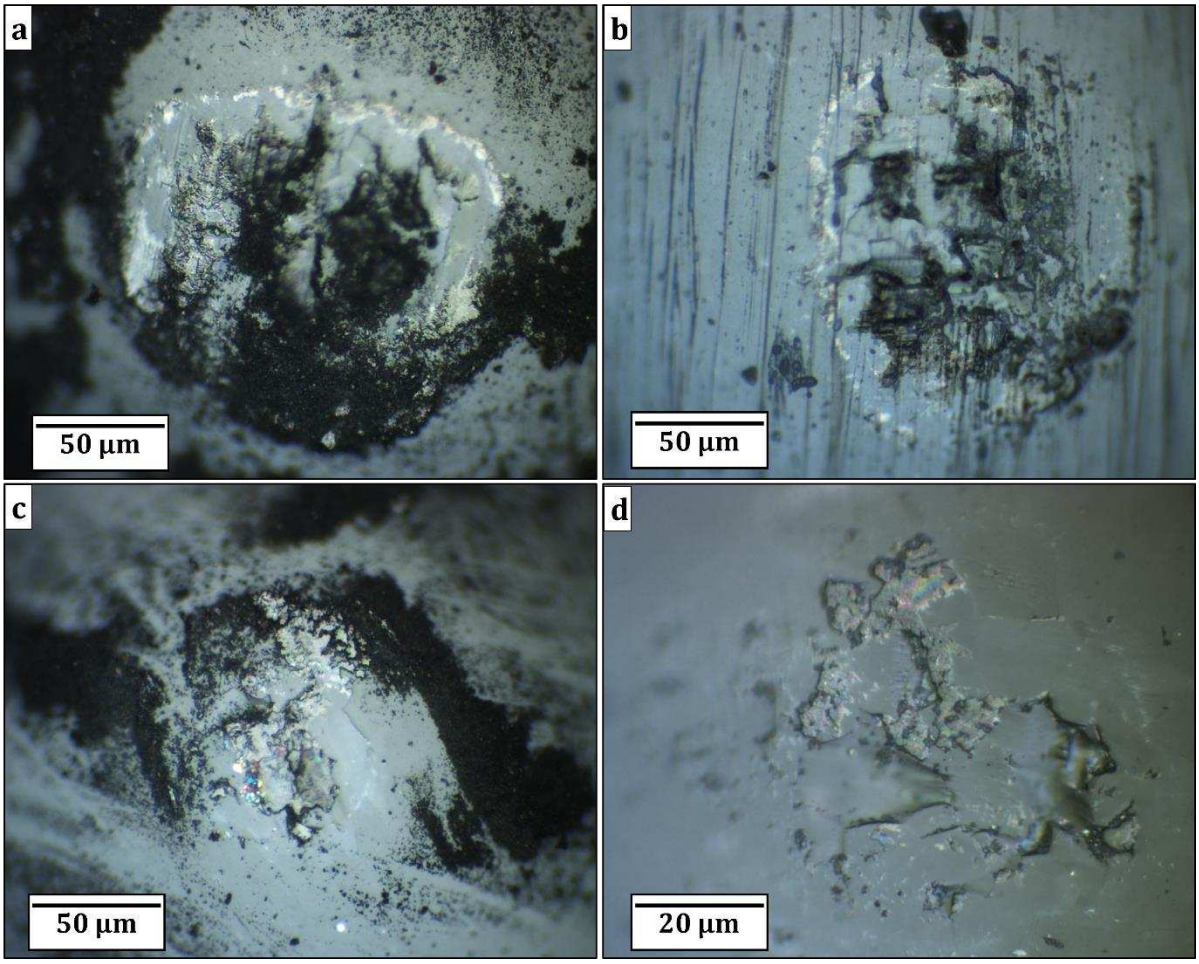


**Fig. 12.** Optical images of the $Al_2O_3$ ball surface after unlubricated sliding against the Maxthal 312 disc ((a) before cleaning and (b) after cleaning) and Maxthal 312-TiC disc ((c) before cleaning and (d) after cleaning) discs for the contact condition 100 rpm for 60 min.

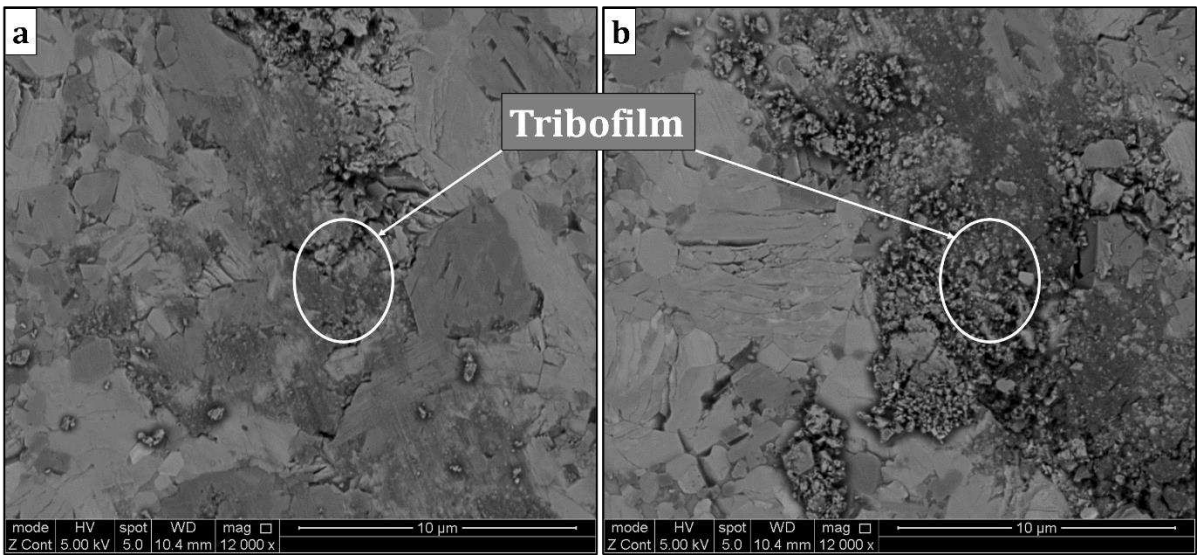


**Fig. 13a.** SEM micrographs of the pre-transition phase of the Maxthal 312/$Al_2O_3$ sliding surface.

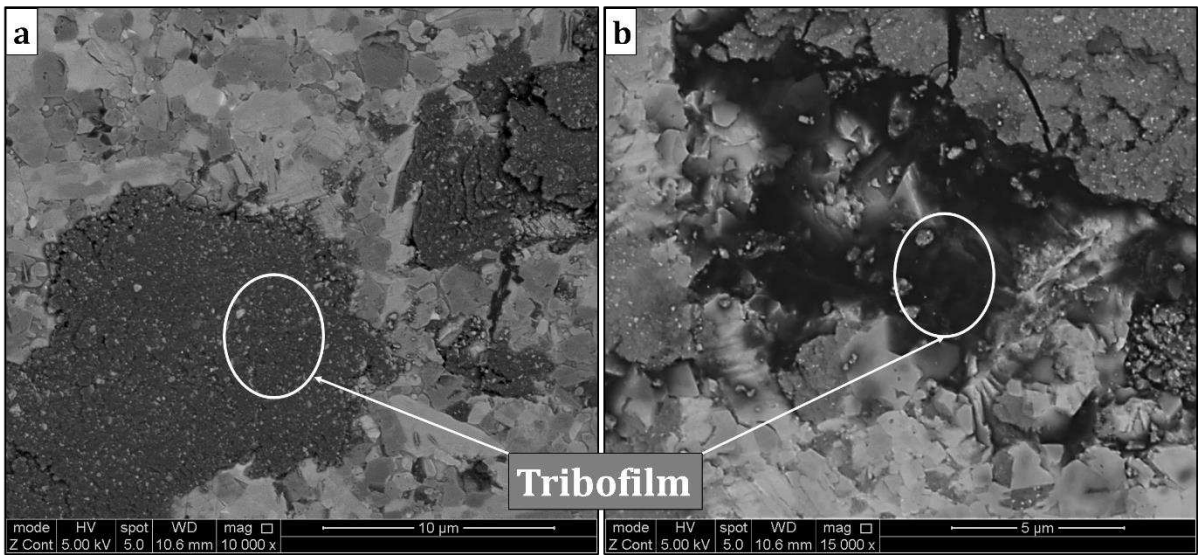


**Fig. 13b.** SEM micrographs of the pre-transition phase of the Maxthal 312-TiC/$Al_2O_3$ sliding surface.

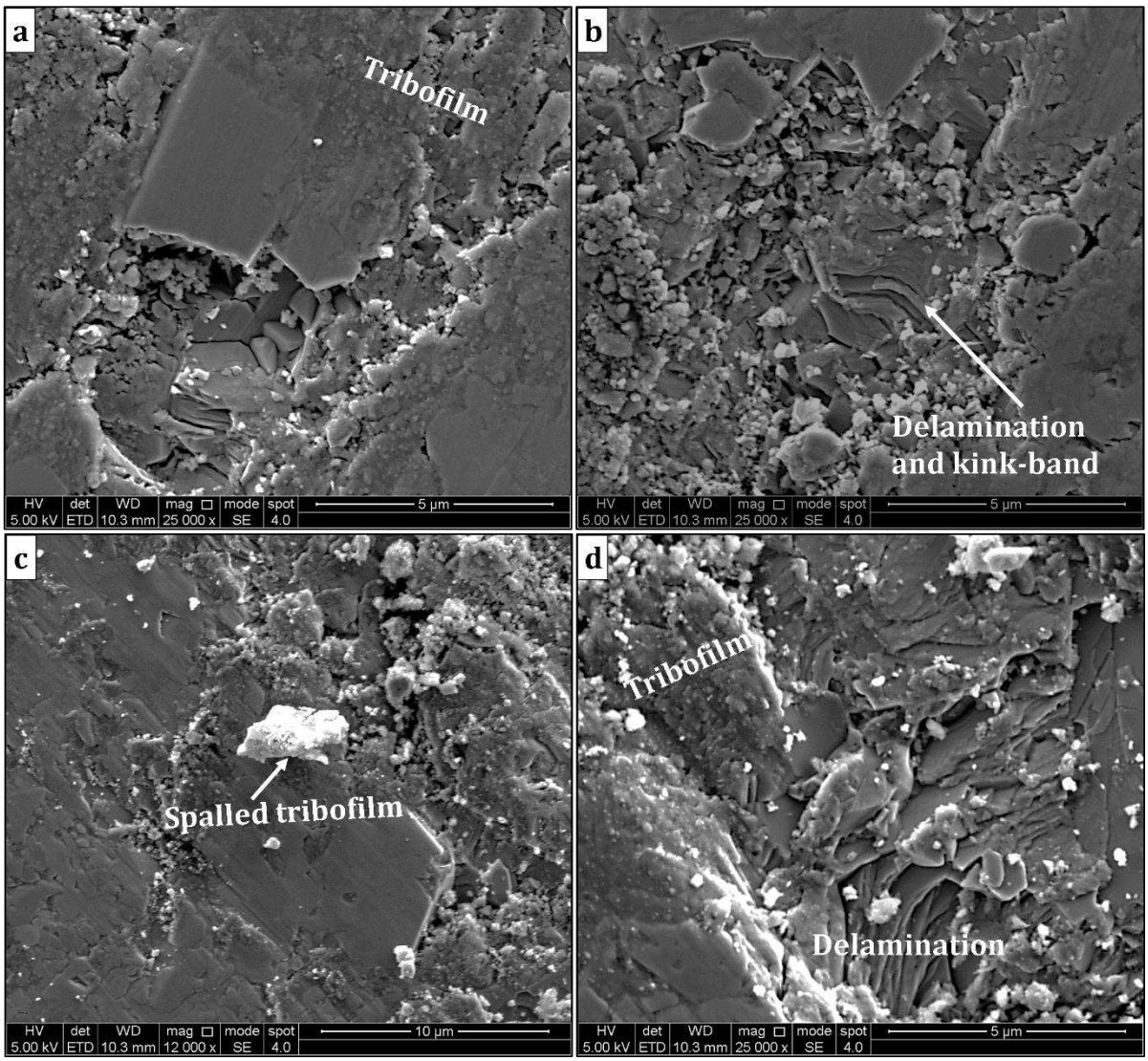


**Fig. 14.** SEM micrographs of the sliding surface of Maxthal 312/$Al_2O_3$ for the contact condition 50 rpm for 60 min (a-b), and 100 rpm for 60 min (c-d). Note: white bits are spalled tribofilms.

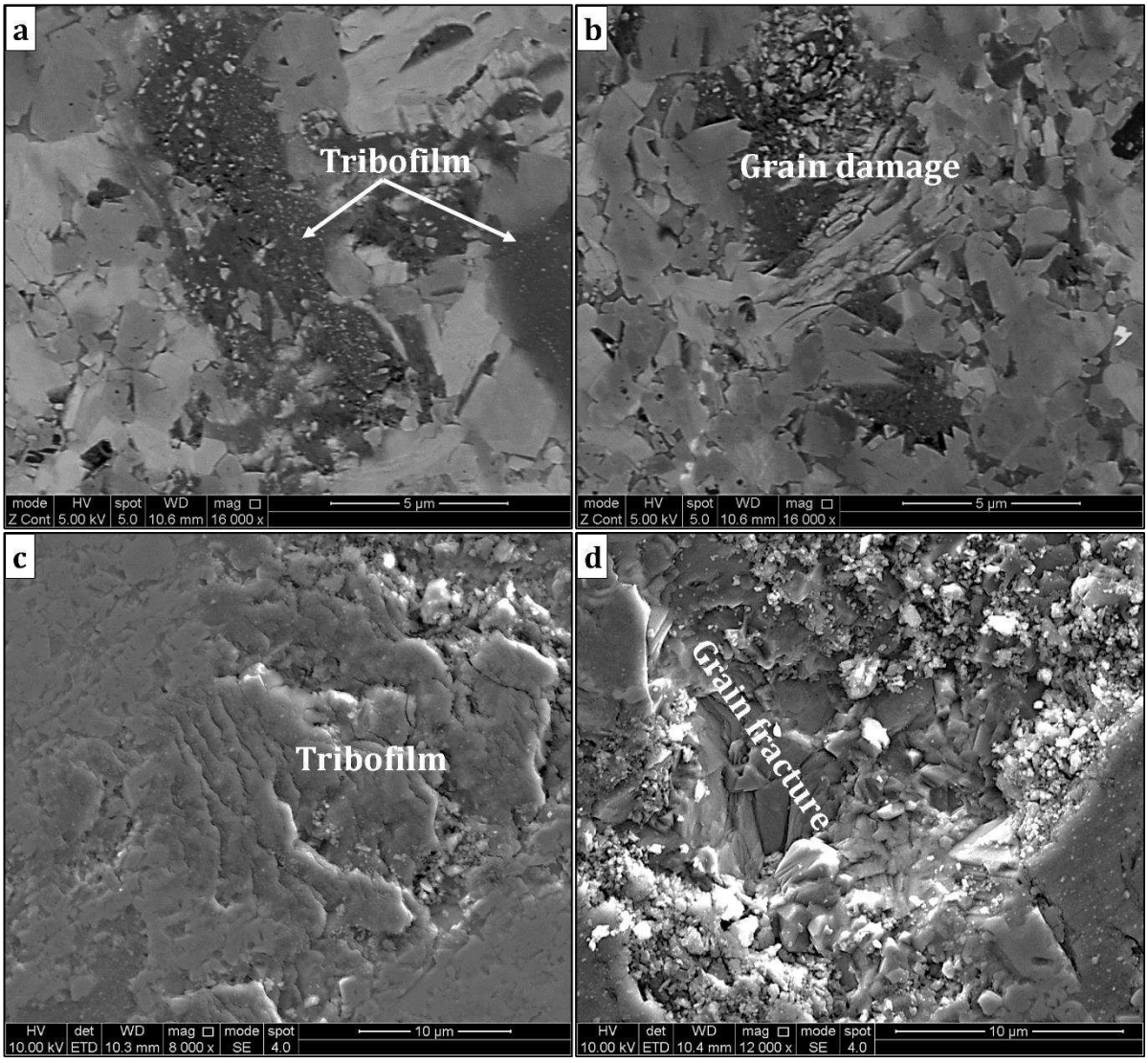


**Fig. 15.** SEM micrographs of the sliding surface of the Maxthal 312-TiC/$Al_2O_3$ for the contact condition 50 rpm for 60 min (a-b), and 100 rpm for 60 min (c-d).

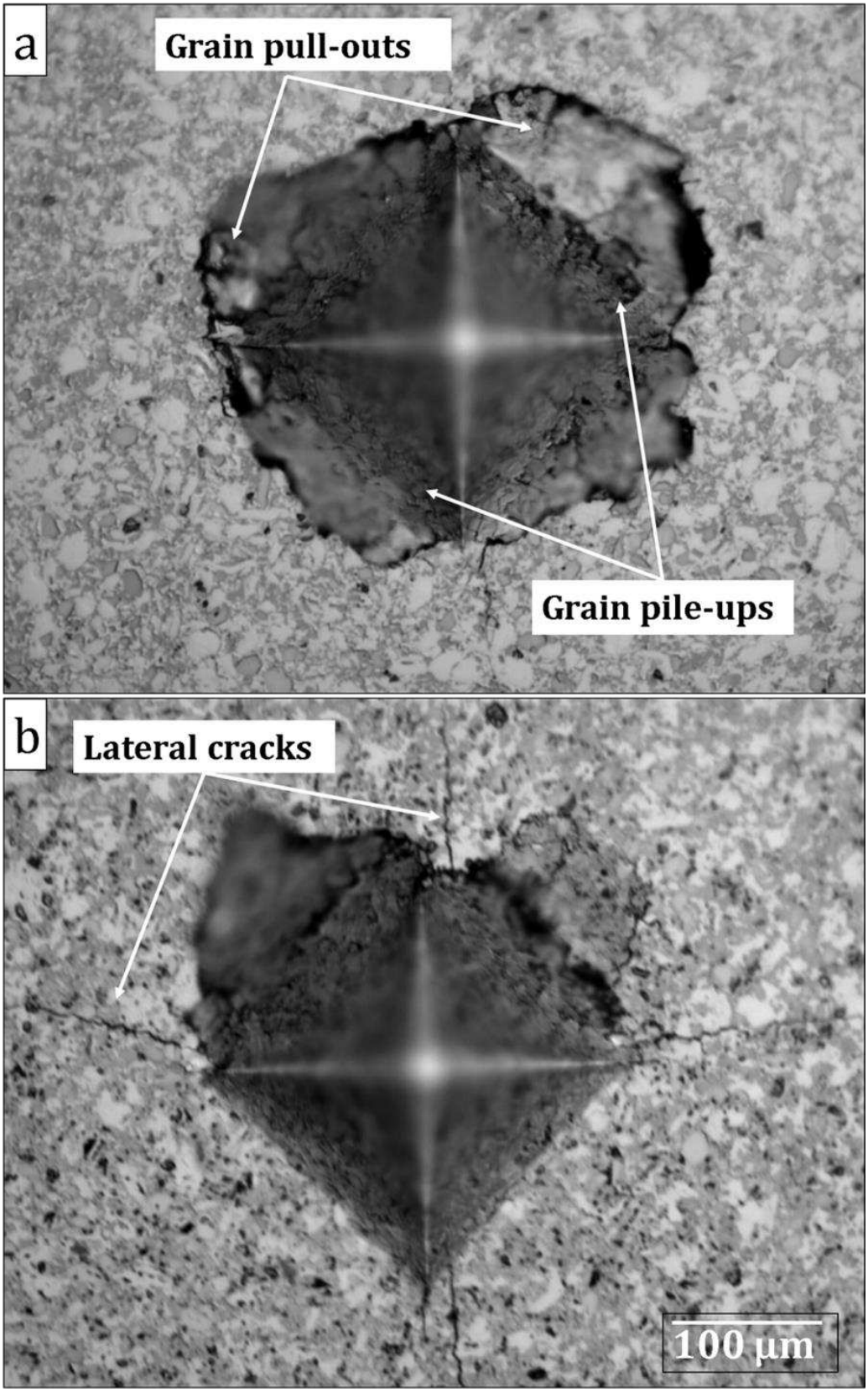


Fig. 16. Optical images showing Vickers induced deformation microstructures: (a) Maxthal 312 and (b) Maxthal 312- TiC using an indentation load of 49 N.

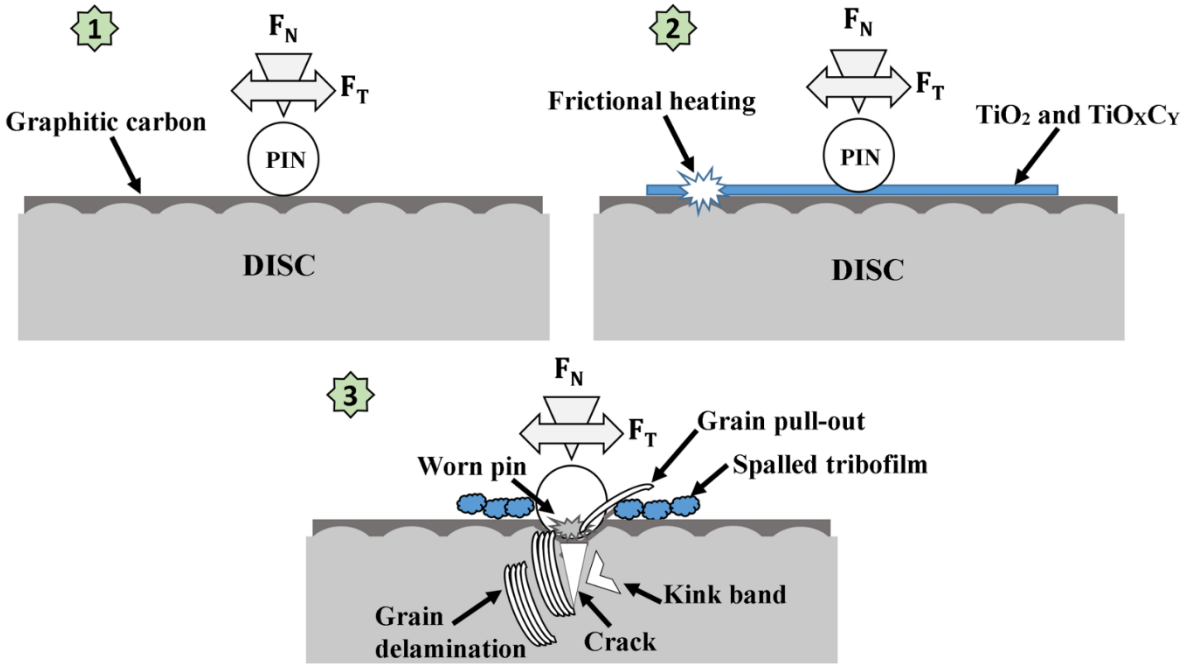


**Fig. 17.** Schematic diagram of the tribo-oxidative to deformation induced wear transition.